Chemical Science

ROYAL SOCIETY OF CHEMISTRY

EDGE ARTICLE

View Article Online
View Journal | View Issue

Cite this: *Chem. Sci.*, 2025, **16**, 15955

All publication charges for this article have been paid for by the Royal Society of Chemistry

Modulating ion migration realizes both enhanced and long-term-stable nanozyme activity for efficient microplastic degradation

Pingping Wan, Guanghui Chen, Jinsong Fan, Wenlong Tan, Xu Li, Lang Chen and Kun Li *

Received 10th June 2025
Accepted 4th August 2025

DOI: 10.1039/d5sc04247j

rsc.li/chemical-science

Degradation of microplastics represents a significant global environmental challenge, necessitating the development of bio-inspired catalysts with superior activity and stability, capable of mimicking natural plastic-degrading enzymes. Although nanozymes possess advantages such as low cost, ready availability, and multienzymatic activities, issues of self-consumption often hinder their practical application. Here, motivated by the acceleration of Li^+ migration for improving the electrochemical reactivity and cycling stability of lithium iron phosphate (LFP), we engineered LFP by introducing Mn^{2+} to expand the lattice structure, resulting in Mn-doped LFP (LFMP) that modulates ion migration in nanozymes. Density functional theory (DFT) calculations reveal that Mn^{2+} doping expands the lattice structure of LFP while narrowing its bandgap, thereby significantly enhancing Li^+ migration rates. Leveraging this design, LFMP exhibits enhanced peroxidase-like activity (3 times higher than that of LFP) and cycling stability (80% activity retention after 5 cycles *versus* 45% for LFP), enabling efficient degradation of microplastics made from polyamide 6, high-density polyethylene, and polypropylene. By exemplifying that the degradation efficiency achieved using LFMP nanozymes significantly exceeds that of traditional methods, we affirm that lattice expansion-driven ion migration may inspire future strategies to circumvent the self-consumption issue while maintaining high catalytic activity in nanozymes.

Introduction

As plastic waste degrades in the environment, it breaks down into particles, fibers, and fragments smaller than 5 mm, collectively known as microplastics.[1–4] Microplastics are persistent pollutants that are widely distributed and can infiltrate the human bloodstream, posing serious health risks.[5–8] To address the challenge of microplastic pollution, various methods such as magnetic separation,[9,10] microbial catabolism,[11,12] photocatalysis,[13–15] and advanced oxidation processes (AOPs)[16,17] have been employed for degradation. Among them, AOPs are particularly promising due to their rapid reaction rates and the high-yield production of hydroxyl radicals ($^{\bullet}OH$), which can effectively mineralize a wide range of plastics.[18] However, challenges remain, such as the poor recyclability of catalysts, which increases the cost of plastic degradation, and the potential for excessive Fe^{2+} to elevate chemical oxygen demand (COD) levels in treated wastewater, leading to secondary pollution.[19,20] Recent advances have also identified plastic-degrading enzymes, such as *Candida antarctica* lipase B (CALB)[21,22] and leaf-branch compost cutinase (LCC),[23–25] which have shown promising progress in plastic degradation. Nonetheless, these enzymes, typically derived from natural microorganisms, suffer from limitations including poorly defined structures, inaccessibility, and instability. Therefore, there is an urgent need to develop alternatives to natural plastic-degrading enzymes with superior catalytic activity and stability for the effective degradation of microplastics.

Given that the generation and utilization of free radicals are involved in the primary mechanism of AOPs, nanozymes,[26,27] as artificial enzymes that mimic natural enzyme activity, are particularly promising due to their reliance on similar free radical mechanisms.[28,29] Besides, nanozymes offer several advantages, including high catalytic activity, stability, and recyclability.[30,31] For example, Fe_3O_4 nanozymes exhibit peroxidase (POD)-like activity, enabling the decomposition of H_2O_2 to produce $^{\bullet}OH$.[32] The radicals efficiently cleave C–C, C–H, and C–O bonds in microplastics, leading to polymer chain fragmentation. Consequently, hydrophilic bare Fe_3O_4 nanoparticles were recently employed to efficiently degrade various microplastics with a removal rate of up to 100%, and these nanoparticles can be easily recycled.[33] However, as research progressed, it was observed that the POD-like catalytic process in Fe_3O_4 nanozymes is accompanied by electron transfer and ion migration of internal atoms. Excessive oxidation of Fe_3O_4 nanozymes leads to a phase transition and a decline in catalytic

State Key Laboratory of Chemo and Biosensing, College of Chemistry and Chemical Engineering, Hunan University, Changsha 410082, P. R. China. E-mail: kunli@hnu.edu.cn

activity, posing a risk of self-depletion.[34] Therefore, addressing the issue of nanozyme self-consumption while maintaining high catalytic activity by modulating the electron transfer and ion migration is of paramount importance.

The issue of material self-consumption is not limited to nanocatalysis but also occurs in electrochemistry. The oxidation and reduction processes of a typical lithium battery material – lithium iron phosphate ($LiFePO_4$, LFP) – are accompanied by the extraction and insertion of Li^+ ions.[35] Therefore, the variable valence states of the Fe element endow LFP with POD-like activity owing to the Fenton-like effect. However, Li^+ migration is constrained by tetrahedral bridging, which limits its free movement, causing LFP to undergo phase transition and catalytic performance instability after numerous cycles.[36–38] To improve the electrochemical reactivity and cycling stability of LFP, conductivity enhancement or crystal structure optimization methods have been employed to accelerate Li^+ migration. Notably, lattice expansion is an effective and promising alternative.[39] We are thus inspired to directly regulate the lattice expansion of LFP by introducing a transition metal element similar to Fe (such as Mn) at Fe sites to enhance the POD-like catalytic activity and long-term cycling stability of LFP. The lattice expansion-accelerated Li^+ migration was further illustrated. The accelerated migration of Li^+ ions in Mn-doped LFP (LFMP) nanozymes enables them to exhibit superior POD-like catalytic activity and cycling stability. Finally, the highly stable LFMP nanozymes were explored to degrade a couple of microplastic pellets with superior degradation efficiency.

Results and discussion

Metal ion-doped lithium iron phosphate with lattice expansion

LFP and LFMP were synthesized *via* co-precipitation (Fig. 1a).[34] The morphology of LFMP was initially examined using scanning electron microscopy (SEM). Fig. 1b shows that LFMP has a rod-like structure with an average length of approximately 300 nm. Energy-dispersive X-ray spectroscopy (EDS) maps indicate that, compared to LFP, elemental Mn is uniformly distributed on the surface of LFMP particles alongside elements Fe, P, and O (Fig. S1–S4). The presence of Mn is further confirmed by X-ray photoelectron spectroscopy (XPS) (Fig. 1c). Fourier transform infrared spectroscopy (FT-IR) reveals stretching and bending vibrations of –OH around 3430 and 1647 cm^{-1}, respectively (Fig. S5), while the PO_4^{3-} peaks of LFP are mainly located at 1300–500 cm^{-1} (Fig. 1d).[40] The introduction of Mn^{2+} does not alter the shape and position of the vibrational peaks. These results substantiate the successful preparation of LFMP.

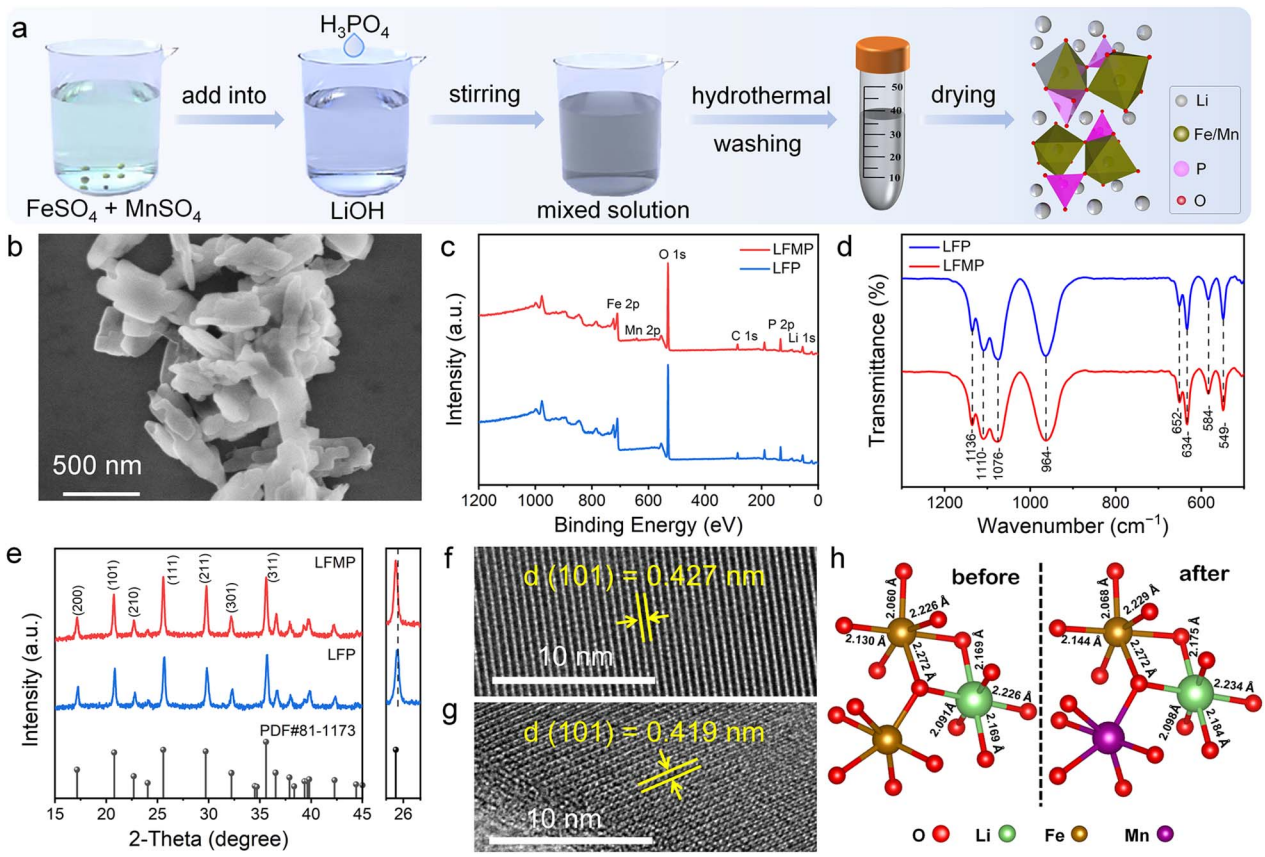

Fig. 1 (a) Schematic illustration of the synthesis of LFMP using the co-precipitation strategy. (b) SEM image of the prepared LFMP. XPS full scan spectra (c), FT-IR (d), and XRD (e) of LFMP and LFP, respectively. HRTEM images of LFMP (f) and LFP (g). Bond lengths of Fe–O and Li–O before and after Mn^{2+} doping (h).

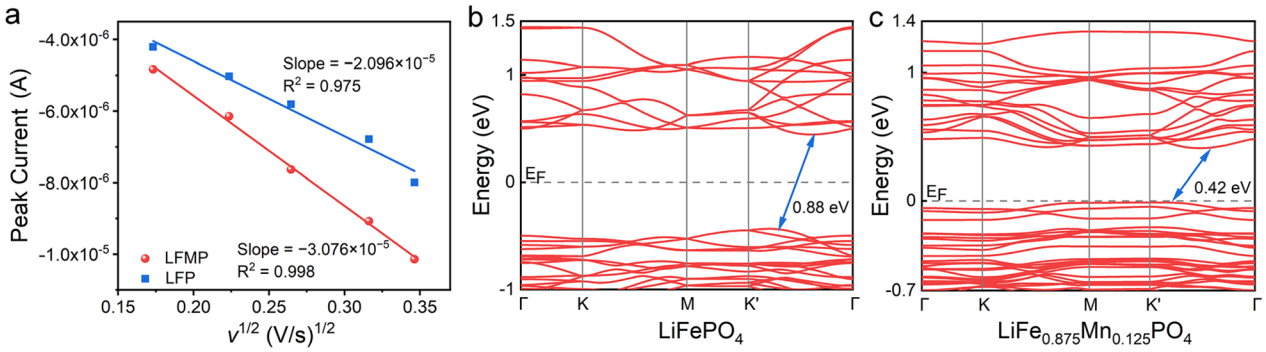

Fig. 2 (a) Plots of the current of the reduction peak (I_p) of LFMP and LFP *versus* the square root of the electrode scanning rate ($v^{1/2}$). Energy band diagrams of LFP (b) and $LiFe_{0.875}Mn_{0.125}PO_4$ (c).

Subsequently, measurements of the crystal plane spacing and calculations of the cell volume were used to analyze whether the introduction of Mn^{2+} could induce lattice expansion of LFP. X-ray diffraction (XRD) measurement demonstrates that the samples are pure, with all diffraction peaks slightly shifting to lower angles upon Mn introduction (Fig. 1e). This shift occurs because the radius of Mn^{2+} (0.83 Å) is slightly larger than that of Fe^{2+} (0.78 Å) in the octahedral coordination environment.[41] The high-angle annular dark-field scanning transmission electron microscopy (HAADF-STEM) images (Fig. 1f, g and S6) reveal distinct lattice fringes, with lattice spacings of 0.427 and 0.419 nm for LFMP and LFP, respectively, corresponding to the (101) plane (PDF#81-1173). This result indicates that the doping of Mn^{2+} can increase the lattice spacing of LFP. Furthermore, density functional theory (DFT) calculations elucidate the effect of Mn^{2+} introduction on the cell volume of $LiFePO_4$. Using LFMP with 12.5% Mn doping as a model, the analysis suggests that Mn^{2+} doping expands the lattice, resulting in a larger unit cell size (Table S1). The Fe–O and Li–O bond lengths of $LiFe_{0.875}Mn_{0.125}PO_4$ and LFP are shown in Fig. 1h. Notably, both Fe–O and Li–O bond lengths increase upon the introduction of Mn^{2+}, reflecting a weakening of Fe–O bond. This weakening is expected to expand the Li^+ migration channel, thereby facilitating its diffusion.

Lattice expansion-accelerated Li^+ migration in LFMP

The diffusion coefficient of Li^+ reflects the Li^+ migration behavior of LF(M)P.[42,43] Therefore, CV curves of LFMP and LFP were tested at different scanning speeds (Fig. S7). The current intensities of their reduction peaks were recorded during negative scanning, and the Li^+ diffusion coefficients were calculated using the Randles–Sevcik equation.[44] Fig. 2a shows that the current intensities of LFMP and LFP have a strong linear relationship with the square root of the scanning speed, indicating that the currents are diffusion-controlled. The Li^+ diffusion coefficients for LFMP and LFP were determined to be 1.04×10^{-6} and 4.83×10^{-7} ($cm^2\ s^{-1}$), respectively, suggesting an increased Li^+ diffusion coefficient in LFP after Mn^{2+} doping.[45]

Additionally, the increased Li^+ diffusion coefficient promotes Li^+ migration in LF(M)P, preventing phase transitions during recycling and enhancing conductivity. Therefore, the band gap widths (E_g) of LFP and $LiFe_{0.875}Mn_{0.125}PO_4$ were calculated to be 0.88 and 0.42 eV, respectively (Fig. 2b and c). A narrower band gap reduces the energy barriers for electron movement, thus enhancing the material's conductivity. The insertion and extraction of Li^+ alter the distribution of Fe species (Fe^{2+} and Fe^{3+}) on the surface. Consequently, we propose that the moderate introduction of Mn^{2+} can enhance the POD-like activity of LFMP by accelerating Li^+ migration, thereby promoting the electron transfer between Fe^{2+} and Fe^{3+}. Meanwhile, the increased Li^+ diffusion coefficient prevents phase transitions in recycled LFMP, contributing to its improved cycling stability.

Enhanced peroxidase-like activity and cycling stability of LFMP

To verify that the accelerated Li^+ migration enhances the POD-like activity and stability of LFP, we compared the catalytic activity of LFP nanozymes before and after Mn^{2+} doping. The POD-like activity of LFMP was examined using the chromogenic reaction of 3,3′,5,5′-tetramethylbenzidine (TMB) and H_2O_2. The solution changes from colorless to blue, exhibiting a distinct absorption peak at 652 nm in the presence of both substrates, TMB and H_2O_2 (Fig. 3a). In the absence of H_2O_2, the solution color does not change, indicating that LFMP exhibits only POD-like activity and not oxidase-like activity. Notably, phosphate solution was used to provide a weakly acidic environment to prevent the dissociation of LFP and LFMP, which interferes with the catalytic activity (Fig. S8 and Section S5.1 in the ESI). In addition, by comparing the POD-like activities of LFP, LFMP, and $LiMnPO_4$ under identical conditions (Fig. S9), we found that the POD-like activity is correlated with the doping content of Mn^{2+} in LFMP, while the contribution of Mn^{2+} in direct peroxidase-like catalysis remains negligible. At a 5% Mn^{2+} doping ratio, LFMP exhibits approximately 3 times higher catalytic activity than pristine LFP. This result is ascribed to the increased affinity of LFP for TMB as LFMP is more negatively charged than LFP, which is also verified by the interesting result that the reaction system does not exhibit chromogenic activity with the anionic ABTS[46] (Fig. S10 and Section S5.3 in the ESI). Meanwhile, explorations with alternative either redox or non-

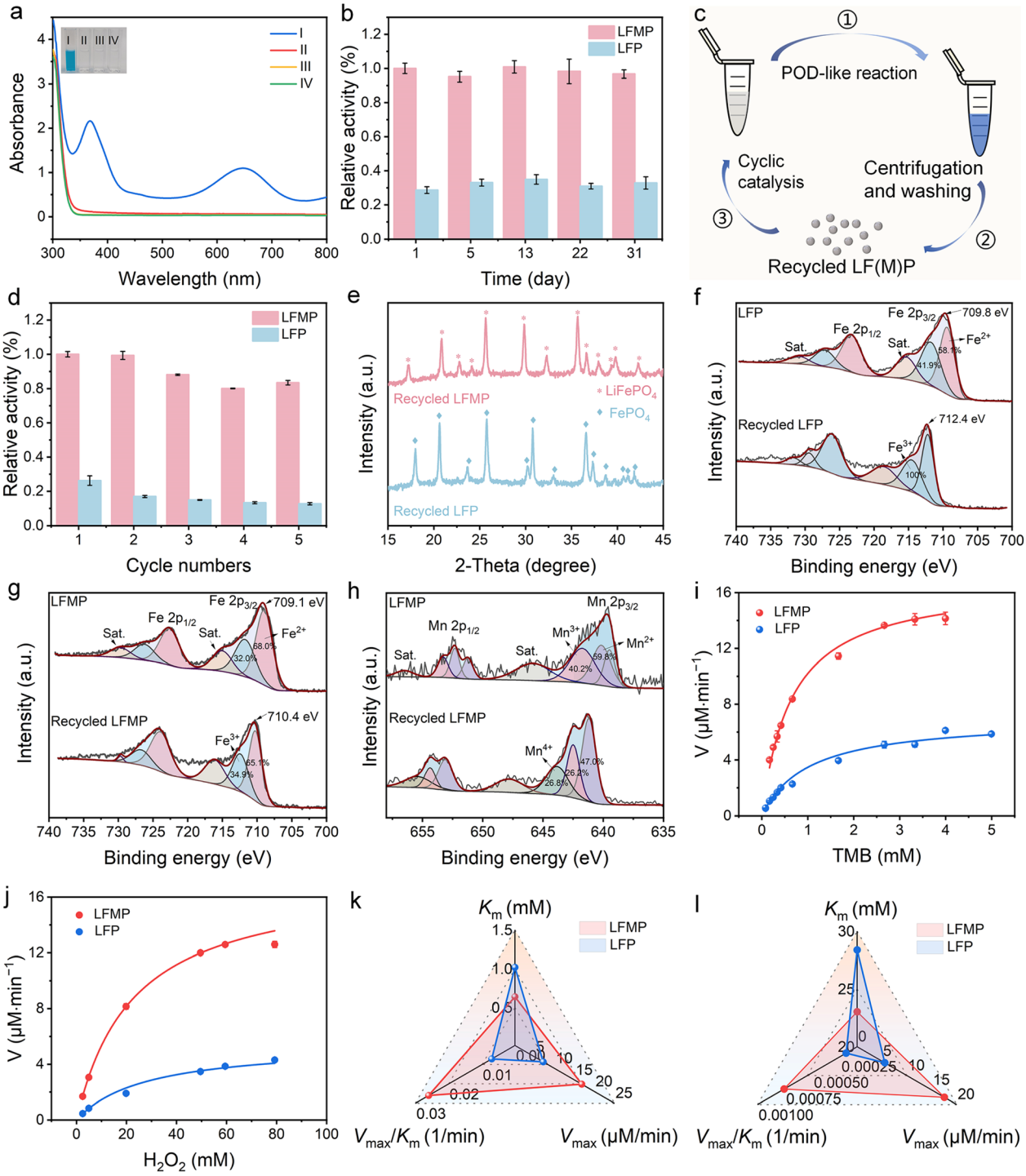

Fig. 3 (a) UV absorption spectra and corresponding photographs (inset) of TMB under different conditions. LFMP + H_2O_2 + TMB (I); LFMP + TMB (II); H_2O_2 + TMB (III); TMB (IV). (b) Relative activity of LFMP and LFP *versus* storage time. (c) The flowchart of the cyclic catalysis process of LF(M)P. (d) Relative activity of LFMP and LFP for TMB oxidation after several catalytic cycles. (e) XRD patterns of cycled LFP and LFMP. Reaction conditions for panels a to d: H_2O_2 (10 mM), TMB (0.42 mM), LFMP or LFP (50 μg mL^{-1}), 0.2 M phosphate solution (pH = 4), 5 min reaction. Fe 2p spectra of LFP (f) and LFMP (g) before reaction and after five cycles of catalysis. (h) Mn 2p spectra of LFMP and recycled LFMP. Michaelis–Menten curves of LFMP and LFP with TMB (i) and H_2O_2 (j) as substrates, respectively. Radar plots of the three parameters (K_m, V_{max}, and V_{max}/K_m) of LFMP and LFP with TMB (k) and H_2O_2 (l) as substrates, respectively. Reaction conditions for panels i to l: LFMP or LFP (10 μg mL^{-1}), 0.2 M phosphate solution (pH = 4), 5 min reaction. For panels i and k: H_2O_2 (50 mM). For panels j and l: TMB (1.68 mM).

redox active metal ion dopants, including Ni^{2+}, Co^{2+}, and Zn^{2+}, resulted in diminished POD-like enzyme activity of LFP (Fig. S11). Interestingly, a decrease in activity also occurred when a larger ion, Na^+, was used instead of Li^+, indicating that ion migration is essential for the enzyme-mimicking catalysis (Fig. S11). In contrast, Mn^{2+} doping, which is favorable for Li^+

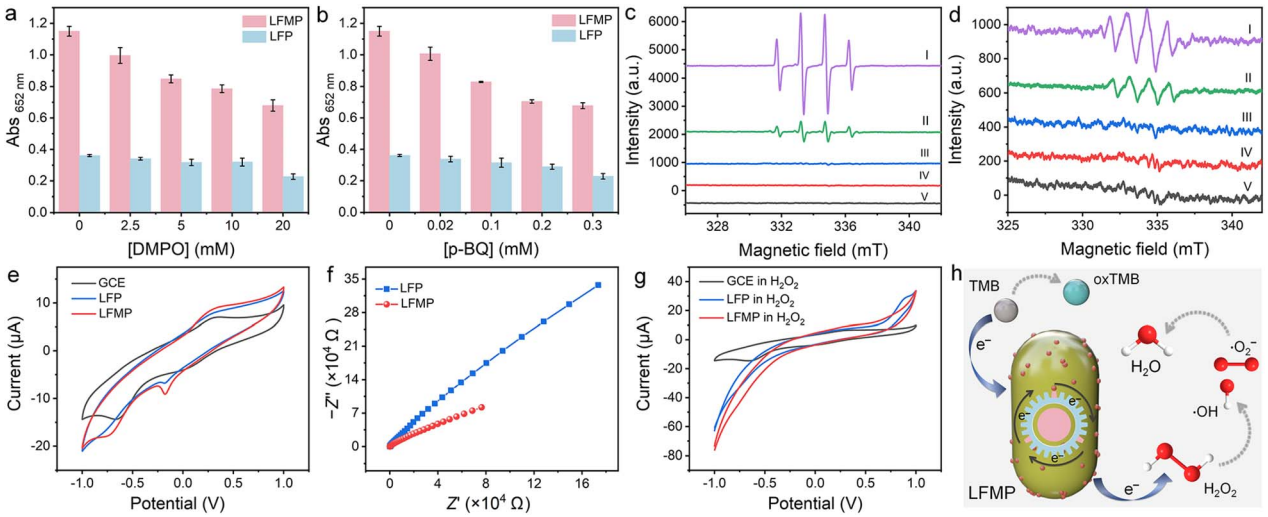

Fig. 4 UV-vis absorption of oxTMB at 652 nm by adding different concentrations of DMPO (a) and *p*-BQ (b). Reaction conditions for panels a and b: H_2O_2 (10 mM), TMB (0.42 mM), LFMP or LFP (50 μg mL^{-1}), 0.2 M phosphate solution (pH = 4), 5 min reaction. ESR spectra of the DMPO/$^{\bullet}OH$ (c) and DMPO/$^{\bullet}O_2^-$ (d) spin adduct of LFMP and LFP in the presence or absence of H_2O_2. For panels c and d: LFMP + DMPO + H_2O_2 (I), LFP + DMPO + H_2O_2 (II), DMPO + H_2O_2 (III), DMPO + LFMP (IV), and DMPO + LFP (V). The solvent is either phosphate solution in panel c or CH_3OH in panel d. Reaction conditions for panels c and d: H_2O_2 (100 mM), DMPO (10 mM), LFMP or LFP (125 μg mL^{-1}), 0.2 M phosphate solution (pH = 4) or CH_3OH, 5 min reaction. (e) Cyclic voltammetry curves of LFMP- and LFP-modified glassy carbon electrodes (GCE) in the absence of H_2O_2. (f) Electrochemical impedance spectra of LFMP and LFP. (g) Cyclic voltammetry curves of the LFMP- and LFP-modified GCE in the presence of H_2O_2. (h) Schematic diagram of the catalytic activity enhancement mechanism of LFMP.

migration, enhances the catalytic performance. These results confirm that the primary role of Mn^{2+} doping in LFMP is to structurally facilitate the Fe^{2+}/Fe^{3+} redox cycle rather than to participate directly in H_2O_2 activation. Consequently, 5% Mn^{2+} doping was selected for subsequent experiments in this study. Unless otherwise specified, LFMP hereinafter refers to $LiFe_{0.95}Mn_{0.05}PO_4$ nanozymes for simplicity.

In addition to catalytic activity, stability is a critical parameter for assessing the performance of POD-like enzymes. For instance, the typical POD-like enzyme, Fe_3O_4, experiences diminished activity upon recycling (Fig. S12), attributed to phase transformation into γ-Fe_2O_3 during prolonged catalysis.[34] We then evaluated the storage stability and the cycling stability of both LFMP and LFP nanozymes. After even one month, both retained nearly unchanged enzymatic activity, indicating the long-term stability of their catalytic properties (Fig. 3b). However, after five reaction cycles, LFP retained only 45% of the initial POD activity; in contrast, LFMP retained approximately 80% of the initial activity, with the observed decrease likely due to unavoidable sample depletion during the cleaning process (Fig. 3c and d). XRD patterns reveal that the composition of recycled LFMP remains unchanged, whereas repeated catalytic cycles induce a distinct structural transformation in LFP. The newly emerged diffraction peaks exhibit perfect correspondence with the reported $FePO_4$ reference patterns in both peak positions and relative intensities (Fig. 3e),[34] providing conclusive evidence for the oxidative conversion of cycled LFP into $FePO_4$. These results demonstrate that LFMP has superior cycling stability compared to LFP.

To further assess the structural stability of LFMP, XPS was employed to investigate the surface chemical state changes of LFP and LFMP particles after multiple catalytic cycles (Fig. 3f–h). In the Fe 2p spectra, the primary peaks at 709.8 and 723.4 eV correspond to Fe $2p_{3/2}$ and Fe $2p_{1/2}$ of LFP, respectively (Fig. 3f). The fitted peaks at binding energies of 709.5 and 723.3 eV are attributed to Fe(II), while those at 711.9 and 727.1 eV correspond to Fe(III); the peaks at 715.4 and 730.8 eV are identified as satellite peaks of Fe 2p. Notably, after five catalytic cycles, the surface Fe^{2+} content of LFP decreased from 58.1% to 0%, suggesting that during successive POD-like reactions occurring on LFP, the surface Fe^{2+} was completely oxidized to Fe^{3+}, which led to a significant attenuation of POD-like activity. In contrast, LFMP exhibited a 0.7 eV reduction in the binding energy of Fe $2p_{3/2}$ compared to LFP, indicating that Mn^{2+} doping results in a higher proportion of Fe(II) on the particle surface (Fig. 3g).[47] After catalysis, the Fe^{2+} proportion in LFMP decreased marginally from 68.0% to 65.1%, while Fe^{3+} increased from 32.0% to 34.9%, indicating partial oxidation during the catalytic process. Analysis of Mn 2p spectra reveals the presence of Mn ions in various oxidation states on the surface of LFMP (Fig. 3h). Specifically, Mn^{2+} decreased from 59.8% to 47.0%, and Mn^{3+} decreased from 40.2% to 26.2%, along with the emergence of Mn^{4+} after catalytic cycles. This oxidation pathway originates from electron transfer between Mn^{2+} and Fe^{3+}, as evidenced by the preserved Fe^{2+} population on cycled LFMP surfaces (Fig. 3g). These findings suggest that the introduction of Mn^{2+} helps regulate the balance between Fe^{2+} and Fe^{3+}, thereby accelerating the electron transfer during the cyclic POD-like process. This charge-balance regulation enables cycled LFMP to retain predominant surface Fe^{2+} species, resulting in only marginal activity loss (Fig. 3d). In stark contrast, undoped LFP suffers from severe Fe^{3+} accumulation and compromised electron

mobility, leading to a significant decrease in POD-like activity (Fig. 3d). These findings unequivocally demonstrate the pivotal role of Mn^{2+} doping in preserving the catalytic integrity of LFMP. Consequently, LFMP exhibits greater structural stability after cycling compared to LFP.

Next, after figuring out the optimal reaction conditions for the POD-like activity of LFMP (Fig. S13), we further assessed its catalytic performance through steady-state kinetics. The reaction rates achieved using both LFMP and LFP increased initially and then stabilized as the concentration of the substrate TMB or H_2O_2 increased (Fig. 3i and j), with the trends being consistent with the Michaelis–Menten equation. A smaller K_m value indicates that the nanozyme has a higher affinity for the substrate. Compared to LFP, these enzymatic kinetic data suggest that LFMP has a higher affinity and reaction rate for TMB and H_2O_2 (Fig. S14 and 3k, l). Notably, LFMP demonstrates superior catalytic activity compared to other reported Fe-based nanozymes (Table S2).

Mechanisms of Li^+ migration to regulate peroxidase-like activity

To elucidate the ROS generation mechanism of LFMP, 5,5-dimethyl-1-pyrroline *N*-oxide (DMPO) and *p*-benzoquinone (*p*-BQ) were employed to capture $^{\bullet}OH$ and $^{\bullet}O_2^-$, respectively. Fig. 4a and b show a significant decrease in absorbance at 652 nm upon the addition of DMPO or *p*-BQ. As the concentration of DMPO or *p*-BQ increases, the absorption peak of oxTMB gradually decreases. A similar decreasing trend in the absorbance of oxTMB catalyzed by LFP is observed, suggesting that $^{\bullet}OH$ and $^{\bullet}O_2^-$ play crucial roles in the oxidation of TMB by both LFMP and LFP. The presence of $^{\bullet}OH$ and $^{\bullet}O_2^-$ was further confirmed by electron spin resonance (ESR).[48] In phosphate solution, DMPO/$^{\bullet}OH$ exhibits a quartet with 1 : 2:2 : 1 relative intensity (Fig. 4c). Notably, the signal intensity of LFMP is higher than that of LFP, indicating that LFMP generates more $^{\bullet}OH$ at the same time. When the reaction solution is methanol, DMPO captures $^{\bullet}O_2^-$ during the reaction of LFMP or LFP with H_2O_2 (Fig. 4d). Consequently, the electron transfer from H_2O_2 on LFMP leads to the production of $^{\bullet}OH$ and $^{\bullet}O_2^-$, which involves the following two main processes:[49]

$$Fe^{2+} + H_2O_2 \rightarrow Fe^{3+} + {}^{\bullet}OH + OH^- \quad (1)$$

$$Fe^{3+} + H_2O_2 \rightarrow Fe^{2+} + {}^{\bullet}O_2^- + 2H^+ \quad (2)$$

As demonstrated in previous experiments, LFMP exhibits stronger POD-like activity than LFP. To reveal the electron transfer process during redox reactions, we investigated the electrochemical behavior of LFMP and LFP. Cyclic voltammetry (CV) curves were recorded for the glassy carbon electrodes (GCE) modified with LFMP or LFP, with the intensity of the redox peaks in the CV curves reflecting the rate of electron transfer between Fe^{2+} and Fe^{3+} (Fig. 4e). The intensity of the redox peaks for electrodes modified with LFMP is stronger than that of LFP, suggesting that Mn^{2+} doping accelerates the electron transfer rate between Fe^{2+} and Fe^{3+}.[50] This finding is consistent with the electrochemical impedance spectroscopy results (Fig. 4f), where the radius of the LFMP electrode is smaller than that of the LFP electrode, indicating that Mn^{2+} doping reduces the charge transfer resistance of LFP. After the addition of H_2O_2, the current of the bare electrode shows minimal changes, while the current intensity of the modified electrode significantly increases, with LFMP showing a pronounced enhancement than LFP (Fig. 4g). Furthermore, the current intensity of the electrode significantly increases with higher H_2O_2 concentrations (Fig. S15).

In summary, the mechanism of POD-like LFMP nanozymes is given in Fig. 4h. Above findings verify that Mn^{2+} doping induces lattice expansion, which facilitates Li^+ migration and consequently enhances the POD-like activity of LFMP compared to LFP. During the catalysis process, LFMP transfers electrons from TMB to the substrate H_2O_2. Particularly, Mn^{2+} doping accelerates the electron transfer between Fe^{2+} and Fe^{3+}, promoting the generation of more $^{\bullet}OH$ or $^{\bullet}O_2^-$ radicals.

Increased efficiency in the degradation of microplastics

Magnetic Fe_3O_4 nanoparticles exhibit POD-like activity and strong adsorption capabilities, not only demonstrating strong affinity for microplastics but also catalytically generating $^{\bullet}OH$, which mediates oxidative cleavage of critical C–C and C–H bonds in polymer chains. This synergistic adsorption–degradation mechanism establishes their broad applicability in the degradation of microplastics.[33,51] However, Fe_3O_4 can undergo chemical changes under high-temperature or highly acidic/alkaline conditions, potentially compromising its performance.[34] This instability mirrors the limitations of LFP (Fig. 3d), whose weak cycling catalytic stability and readily deactivated POD-like activity hinder its practical application in microplastic degradation. In contrast, LFMP achieves high cycling stability and POD-like activity by facilitating Li^+ ion migration. Moreover, LFMP is composed of abundant and low-cost raw materials and is free of heavy metals, rendering it environmentally benign. More importantly, we found that LFMP with POD-like activity can still produce $^{\bullet}OH$ at 180 °C, indicating that higher temperatures do not compromise the structure and catalytic activity of LFMP (Fig. S16). Therefore, although the negatively-charged and hydrophilic LFMP cannot adsorb negatively-charged and hydrophobic MPs,[33] its enhanced catalytic activity inspired us to use LFMP as a potential alternative to Fe_3O_4 for plastic degradation. In this work, LFMP with POD-like activity was further employed to degrade polyamide 6 (PA6), high density polyethylene (HDPE), and polypropylene (PP) microplastics (Fig. 5a), which were identified by optical microscopy as irregular spherical particles with sizes ranging from 0.5 to 4.5 mm (Fig. S17). First, we optimized the microplastic degradation efficiency by varying LFMP concentration, reaction temperature, pH, H_2O_2 concentration, reaction time, and microplastic concentration (Fig. S18).

When other external conditions were held constant, we compared the degradation efficiencies of MPs treated by four methods: heat treatment (heat), nanomaterial heat treatment (LFMP), H_2O_2 treatment (H_2O_2), and nanozymatic catalysis

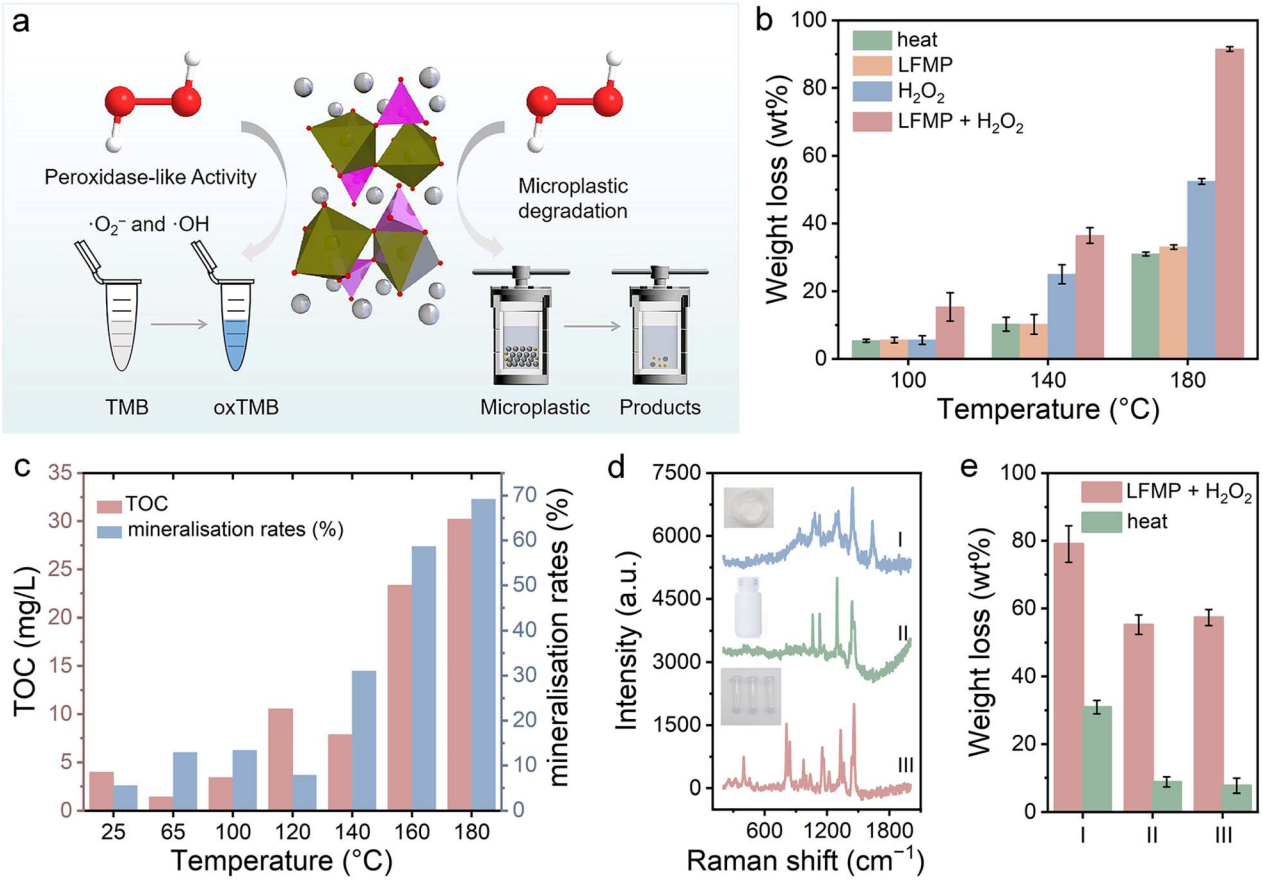

Fig. 5 (a) Scheme of the degradation of MPs using peroxidase-like LFMP nanozymes. (b) Degradation efficiency of PA6 treated by various methods at different temperatures. (c) TOC and mineralization rate of the degraded solution of PA6 by LFMP nanozymes at different temperatures. Reaction conditions for panels b and c: LFMP (0.5 mg mL^{-1}), H_2O_2 (250 mM), PA6 (5 mg mL^{-1}), 0.2 M phosphate solution (pH 4), 8 h reaction. (d) Raman spectra of nylon pipes (I), plastic bottles (II), and centrifuge tubes (III). (e) Degradation of nylon pipes (I), plastic bottles (II), and centrifuge tubes (III) through different treatments. Reaction conditions for panel e: LFMP (0.5 mg mL^{-1}), H_2O_2 (250 mM), real-world plastics (5 mg mL^{-1}), 0.2 M phosphate solution (pH 4), 180 °C for I and II; 160 °C for III, 8 h reaction.

treatment (LFMP + H_2O_2). Notably, the degradation efficiency progressively increases with rising temperature (Fig. 5b and S18b). At temperatures below the glass transition temperature (T_g) of plastics, the scission of polymer chains becomes less favorable.[52,53] Even in the presence of nanozymes, the catalytic process remains inefficient under such conditions due to their reduced activity at low temperatures. The limited radical concentration consequently restricts the nanozyme-catalyzed plastic degradation reaction. At each reaction temperature, the degradation efficiency of PA6 by heat is lowest; however, the degradation efficiency of MPs is enhanced if H_2O_2 is introduced and even higher if LFMP nanozymes are used (Fig. 5b). When PA6 is treated with the nanozyme at 180 °C for 8 h, the weight loss reaches 91.5%, which is much higher than that observed for heat (30.9%), LFMP (33.0%), and H_2O_2 (52.4%). Moreover, we calculated the mineralization rate (the percentage of plastic completely converted into CO_2, H_2O_2, and inorganic small molecules) of PA6 microplastic degradation by testing the total organic carbon (TOC) content in the degradation solution (Fig. 5c and Section S10.2 in the ESI). The highest mineralization rate of PA6 achieved by the nanozyme was 77.0% after 12 h of reaction at 180 °C (Fig. S19). In addition, the degradation products of PA6 were analyzed by GC-MS, as shown in Table S3, mainly including aromatic hydrocarbons, ketones, esters, and amides. The non-toxicity of the degradation products was verified by the normal growth of wheat seeds (Fig. S20). Meanwhile, the LFMP nanozyme could be used to degrade HDPE and PP powders, resulting in weight losses of 66.7% and 78.0%, respectively (Fig. S21). Notably, the degradation efficiency of MPs by LFMP nanozymes represents a significant advancement compared to previous methods for degrading microplastics (Table S4). More importantly, the proposed nanozymes are cost-effective to synthesize and stable during use.

Finally, the degradation of some daily-life plastics was evaluated to verify the practicability of LFMP. Nylon pipes, plastic bottles, and centrifuge tubes were sliced prior to the identification of their compositions by Raman spectroscopy (Fig. 5d), which were consistent with those of PA6, HDPE, and PP standard samples (Fig. S22). The degradation efficiencies of nylon tubes, plastic bottles, and centrifuge tubes by the nanozyme reached 79.0%, 55.2%, and 57.3% weight loss, respectively (Fig. 5e). In contrast, the degradation efficiencies of nylon

tubes, plastic bottles, and centrifuge tubes were only 30.9%, 8.8%, and 7.7% weight loss after heat treatment.

Conclusion

In this study, we successfully engineered LFP by substituting Fe sites with large-radius Mn^{2+} ions to synthesize Mn-doped LFP, which exhibits superior POD-like activity. This substitution resulted in lattice expansion, significantly improving both the natural enzyme-like activity and cycling stability compared to pristine LFP. The lattice expansion facilitates the migration of Li^+ ions, thereby enhancing the Li^+ diffusion coefficient and further accelerating electron transfer between Fe^{2+} and Fe^{3+}. This modulation of ion migration in nanozymes not only addresses the self-consumption issue but also maintains high catalytic capability. LFMP demonstrated highly efficient degradation of plastic micropellets and real-world fragments including PA6, HDPE, and PP. This work highlights the potential of LFMP as a promising nanozyme for the degradation of microplastics, offering a significant contribution to the research and application of nanozymes in addressing environmental challenges.

Author contributions

Pingping Wan: investigation, methodology, formal analysis, data curation, visualization, writing – original draft. Guanghui Chen: formal analysis. Jinsong Fan: investigation, data curation. Wenlong Tan: investigation. Xu Li: methodology. Lang Chen: software, validation. Kun Li: conceptualization, resources, supervision, writing – original draft, writing – review & editing.

Conflicts of interest

There are no conflicts to declare.

Data availability

Supplementary information, including extensive methods, figures, and additional results on materials characterization, reaction conditions optimization, and data analysis, is available. See DOI: **https://doi.org/10.1039/d5sc04247j**.

Acknowledgements

This research was financially supported by the National Natural Science Foundation of China (No. 22074038) and the Fundamental Research Funds for the Central Universities. The authors thank the Analytical Instrumentation Center of Hunan University for SEM, TEM, XPS, Raman, and ESR measurements.

Notes and references

1 R. C. Thompson, W. Courtene-Jones, J. Boucher, S. Pahl, K. Raubenheimer and A. A. Koelmans, *Science*, 2024, **386**, eadl2746.
2 W. Huang and X. Xia, *Science*, 2024, **385**, 933–935.
3 X. F. Wei, W. Yang and M. S. Hedenqvist, *Nat. Commun.*, 2024, **15**, 2052.
4 M. Zandieh, E. Griffiths, A. Waldie, S. Li, J. Honek, F. Rezanezhad, P. Van Cappellen and J. Liu, *Exploration*, 2024, **4**, 20230018.
5 T. Wang, S. Zhao, L. Zhu, J. C. McWilliams, L. Galgani, R. M. Amin, R. Nakajima, W. Jiang and M. Chen, *Nat. Rev. Earth Environ.*, 2022, **3**, 795–805.
6 Z. Liu, A. Sokratian, A. M. Duda, E. Xu, C. Stanhope, A. Fu, S. Strader, H. Li, Y. Yuan, B. G. Bobay, J. Sipe, K. Bai, I. Lundgaard, N. Liu, B. Hernandez, C. Bowes Rickman, S. E. Miller and A. B. West, *Sci. Adv.*, 2023, **9**, eadi8716.
7 N. Qian, X. Gao, X. Lang, H. Deng, T. M. Bratu, Q. Chen, P. Stapleton, B. Yan and W. Min, *Proc. Natl. Acad. Sci. U. S. A.*, 2024, **121**, e2300582121.
8 D. He, G. Huang, Z. Zhou, Q. Hu, J. Ding, J. Wu, M. Li, X. Ruan, X. Jiao and Y. Xie, *Adv. Funct. Mater.*, 2024, 2419801.
9 A. Misra, C. Zambrzycki, G. Kloker, A. Kotyrba, M. H. Anjass, I. Franco Castillo, S. G. Mitchell, R. Guttel and C. Streb, *Angew. Chem., Int. Ed.*, 2020, **59**, 1601–1605.
10 M. Urso, M. Ussia, X. Peng, C. M. Oral and M. Pumera, *Nat. Commun.*, 2023, **14**, 6969.
11 S. Yoshida, K. Hiraga, T. Takehana, I. Taniguchi, H. Yamaji, Y. Maeda, K. Toyohara, K. Miyamoto, Y. Kimura and K. Oda, *Science*, 2016, **351**, 1196–1199.
12 Z. Zhang, H. Peng, D. Yang, G. Zhang, J. Zhang and F. Ju, *Nat. Commun.*, 2022, **13**, 5360.
13 Y. Miao, Y. Zhao, J. Gao, J. Wang and T. Zhang, *J. Am. Chem. Soc.*, 2024, **146**, 4842–4850.
14 M. Li and S. Zhang, *ACS Catal.*, 2024, **14**, 2949–2958.
15 Q. Hu, Z. Zhang, D. He, J. Wu, J. Ding, Q. Chen, X. Jiao and Y. Xie, *J. Am. Chem. Soc.*, 2024, **146**, 16950–16962.
16 I. A. Ricardo, E. A. Alberto, A. H. Silva Júnior, D. L. P. Macuvele, N. Padoin, C. Soares, H. Gracher Riella, M. C. V. M. Starling and A. G. Trovó, *Chem. Eng. J.*, 2021, **424**, 130282.
17 X. Kong, A. Zhou, X. Chen, X. Cheng, Y. Lai, C. Li, Q. Ji, Q. Ji, J. Kong, Y. Ding, F. Zhu and H. He, *Sci. Total Environ.*, 2024, **917**, 170420.
18 Z. Yang, Y. Li and G. Zhang, *Chemosphere*, 2024, **357**, 141939.
19 H. Zhao, J. Peng, Z. Chen, Y. Zhou, M. Xu, H. Zhang and X. Zhao, *Chem. Eng. J.*, 2024, **497**, 154831.
20 J. Chen, J. Wu, P. C. Sherrell, J. Chen, H. Wang, W. x. Zhang and J. Yang, *Adv. Sci.*, 2022, **9**, 2103764.
21 K. Swiderek, S. Velasco-Lozano, M. A. Galmes, I. Olazabal, H. Sardon, F. Lopez-Gallego and V. Moliner, *Nat. Commun.*, 2023, **14**, 3556.
22 D. H. Hwang, M. E. Lee, B. H. Cho, J. W. Oh, S. K. You, Y. J. Ko, J. E. Hyeon and S. O. Han, *Sci. Total Environ.*, 2022, **842**, 156890.
23 Y. Cui, Y. Chen, J. Sun, T. Zhu, H. Pang, C. Li, W. C. Geng and B. Wu, *Nat. Commun.*, 2024, **15**, 1417.
24 Y. Zheng, Q. Li, P. Liu, Y. Yuan, L. Dian, Q. Wang, Q. Liang, T. Su and Q. Qi, *ACS Catal.*, 2024, **14**, 3627–3639.

25 M. Ismail, A. Abouhmad, N. Warlin, S.-H. Pyo, O. E. Örn, B. Al-Rudainy, C. Tullberg, B. Zhang and R. Hatti-Kaul, *Green Chem.*, 2024, **26**, 3863–3873.
26 Y. Zhang, G. Wei, W. Liu, T. Li, Y. Wang, M. Zhou, Y. Liu, X. Wang and H. Wei, *Nat. Rev. Methods Primers*, 2024, **4**, 37.
27 L. Jiao, H. Yan, Y. Wu, W. Gu, C. Zhu, D. Du and Y. Lin, *Angew. Chem., Int. Ed.*, 2019, **59**, 2565–2576.
28 M. Zandieh and J. Liu, *Adv. Mater.*, 2024, **36**, 2211041.
29 T. Li, Y. Wang, W. Liu, H. Fei, C. Guo and H. Wei, *Angew. Chem., Int. Ed.*, 2023, **62**, e202212438.
30 D. Yan, L. Jiao, C. Chen, X. Jia, R. Li, L. Hu, X. Li, Y. Zhai, P. E. Strizhak, Z. Zhu, J. Tang and X. Lu, *Nano Lett.*, 2024, **24**, 2912–2920.
31 S. Li, Z. Zhou, Z. Tie, B. Wang, M. Ye, L. Du, R. Cui, W. Liu, C. Wan, Q. Liu, S. Zhao, Q. Wang, Y. Zhang, S. Zhang, H. Zhang, Y. Du and H. Wei, *Nat. Commun.*, 2022, **13**, 827.
32 Z. Zhang, X. Zhang, B. Liu and J. Liu, *J. Am. Chem. Soc.*, 2017, **139**, 5412–5419.
33 M. Zandieh and J. Liu, *Angew. Chem., Int. Ed.*, 2022, **61**, e202212013.
34 H. Dong, W. Du, J. Dong, R. Che, F. Kong, W. Cheng, M. Ma, N. Gu and Y. Zhang, *Nat. Commun.*, 2022, **13**, 5365.
35 X. X. Zhao, X. T. Wang, J. Z. Guo, Z. Y. Gu, J. M. Cao, J. L. Yang, F. Q. Lu, J. P. Zhang and X. L. Wu, *Adv. Mater.*, 2024, 2308927, DOI: **10.1002/adma.202308927**.
36 L. Dong, L. Nie and W. Liu, *Adv. Mater.*, 2020, **32**, 1908494.
37 Z. Wang, H. Xu, Z. Liu, M. Jin, L. Deng, S. Li and Y. Huang, *J. Mater. Chem. A*, 2023, **11**, 9057–9065.
38 M. Shan, C. Dang, K. Meng, Y. Cao, X. Zhu, J. Zhang, G. Xu and M. Zhu, *Mater. Today*, 2024, **73**, 130–150.
39 G. Pagot, F. Bertasi, G. Nawn, E. Negro, G. Carraro, D. Barreca, C. Maccato, S. Polizzi and V. Di Noto, *Adv. Funct. Mater.*, 2015, **25**, 4032–4037.
40 X. Zhi, G. Liang, L. Wang, X. Ou, L. Gao and X. Jie, *J. Alloys Compd.*, 2010, **503**, 370–374.
41 G. A. dos Santos Junior, V. D. S. Fortunato, F. G. Gandra, C. C. Nascentes, G. G. Silva, P. F. R. Ortega and R. L. Lavall, *J. Energy Storage*, 2023, **74**, 109112.
42 Y. Hu, X. Wang, P. Li, J. Chen and S. Chen, *Sci. China: Chem.*, 2023, **66**, 3297–3306.
43 F. Jiang, K. Qu, M. Wang, J. Chen, Y. Liu, H. Xu, Y. Huang, J. Li, P. Gao, J. Zheng, M. Chen and X. Li, *Sustainable Energy Fuels*, 2020, **4**, 2741–2751.
44 L. Chen, Y. Meng, Y. Wang, P. Wang, J. Li, Q. Lv, Z. Zhang, Q. Zhao and D. Xiao, *Inorg. Chem. Front.*, 2021, **8**, 5240–5250.
45 L. Yang, Y. Tian, J. Chen, J. Gao, Z. Long, W. Deng, G. Zou, H. Hou and X. Ji, *J. Mater. Chem. A*, 2021, **9**, 24686–24694.
46 P. Zhang, D. Sun, A. Cho, S. Weon, S. Lee, J. Lee, J. W. Han, D. P. Kim and W. Choi, *Nat. Commun.*, 2019, **10**, 940.
47 C. Zhang, X. Zhang, Y. Ye, P. Ni, C. Chen, W. Liu, B. Wang, Y. Jiang and Y. Lu, *Analyst*, 2022, **147**, 238–246.
48 J. Wang, J. Qin, C. Yang and Y. Hu, *Chemosphere*, 2023, **340**, 139841.
49 H. Zhuang, S. Shan, J. Guo, Y. Han and C. Fang, *Environ. Sci. Pollut. Res. Int.*, 2017, **24**, 27136.
50 Z. Mu, S. Wu, J. Guo, M. Zhao and Y. Wang, *ACS Sustainable Chem. Eng.*, 2022, **10**, 2984–2993.
51 J. Lu, Y. Qiu, L. Zhang, J. Wang, C. Li, P. Wang and L. Ren, *J. Hazard. Mater.*, 2024, **467**, 133689.
52 T.-P. Vo, J. Rintala, L. Dai, W.-D. Oh and C. He, *Water Res.*, 2023, **245**, 120672.
53 L. Wang, W. Cheng, X. Yang, R. Wang, R. Liu, Y. Zhu, Y. Yi, Y. Tang and Z. Wang, *Polym. Degrad. Stab.*, 2023, **215**, 110450.